Accepted Manuscript

Sensitivity assessment of optimal solution in aerodynamic design optimisation using SU2

Guangda Yang, Andrea Da Ronch, Jernej Drofelnik, Zheng-Tong Xie

PII: S1270-9638(18)31149-0
DOI: https://doi.org/10.1016/j.ast.2018.08.012
Reference: AESCTE 4711

To appear in: *Aerospace Science and Technology*

Received date: 29 May 2018
Revised date: 7 August 2018
Accepted date: 10 August 2018

Please cite this article in press as: G. Yang et al., Sensitivity assessment of optimal solution in aerodynamic design optimisation using SU2, *Aerosp. Sci. Technol.* (2018), https://doi.org/10.1016/j.ast.2018.08.012

Sensitivity Assessment of Optimal Solution in Aerodynamic Design Optimisation using SU2

Guangda Yang[a], Andrea Da Ronch[a,*], Jernej Drofelnik[a], Zheng-Tong Xie[a]

[a] *Faculty of Engineering and the Environment*
University of Southampton, Southampton SO17 1BJ, U.K.

Abstract

Computational fluid dynamics has become the method of choice for aerodynamic shape optimisation of complex engineering problems. However, the sensitivity of the final aerodynamic shape to numerical parameters has been largely underestimated to date. The purpose of this work is to investigate the influence that numerical parameters have on the optimisation results for two aerofoil problems (NACA 0012 and RAE 2822) in transonic flow, and to provide compact guidelines for best practice. Numerical parameters include: a) two parameterisation methods, Hicks–Henne bump functions and free–form deformation; b) numerical settings related to the tuning of each parameterisation method; and c) closure coefficients of Spalart–Allmaras (SA) turbulence model. All optimisations were performed using the open–source software tool SU2, and gradients were computed using the continuous adjoint method. It was found that: a) the optimisation result of NACA 0012 aerofoil exhibits strong dependence on all numerical parameters investigated, whereas the optimal design of RAE 2822 aerofoil is insensitive to those numerical settings; b) the degree of sensitivity reflects the difference in the design space, particularly of the local curvature on the optimised shape; c) the closure coefficients of SA model affect the final optimisation performance, raising the need for a good calibration of the turbulence model.

Keywords: aerodynamic shape optimisation, SU2, uncertainty,

*Corresponding author. AIAA Senior Member.
Email address: A.Da-Ronch@soton.ac.uk (Andrea Da Ronch)

gradient–based optimisation, Hicks–Henne bump function, free–form deformation

Nomenclature

M	Mach number
n_{dv}	Number of design variables
C_d	Drag coefficient
C_l	Lift coefficient
C_m	Pitching moment coefficient
C_p	Pressure coefficient
Re	Reynolds number
α	Angle of Attack

Abbreviations

2D	Two–Dimensional
3D	Three–Dimensional
ADODG	Aerodynamic Design Optimisation Discussion Group
ASO	Aerodynamic Shape Optimisation
CFD	Computational Fluid Dynamics
FFD	Free–Form Deformation
HHBF	Hicks–Henne Bump Function
KKT	Karush–Kuhn–Tucker
RANS	Reynolds–Averaged Navier–Stokes
SA	Spalart–Allmaras
SLSQP	Sequential Least SQuares Programming

1. Introduction

The issue of aviation carbon emissions has raised public concern increasingly over the years. To achieve fuel burn reduction, aircraft manufacturers have made

much efforts on developing new technologies. In particular, one key aspect is improving aerodynamic performance through drag minimisation. With the rapid development of Computational Fluid Dynamics (CFD), numerical optimisation has shown the potential to be a powerful tool in fulfilling the aforementioned task. By integrating a CFD solver with an optimisation algorithm, geometry parameterisation and mesh deformation techniques, designers are enabled to perform Aerodynamic Shape Optimisation (ASO) with ease.

A number of ASO frameworks have been developed in the research community over the past few years. Various approaches and tools have been used for each component of an ASO framework. For example, methods of choice for geometry parameterisation were Free–Form Deformation (FFD) [1, 2], B–splines [2, 3], Radial Basis Functions (RBFs) [4, 5], CAD shape [6], PARSEC [7] and Singular Value Decomposition (SVD) [8], among others. For benchmarking purpose, the AIAA Aerodynamic Design Optimisation Discussion Group (ADODG) has established a set of aerodynamic optimisation problems with increasing complexity, ranging from single–point aerofoil optimisation to multi–point wing–body–tail optimisation. A number of research groups have presented their results and highlighted their own contributions. Reference [9] selected six shape parameterisation techniques and investigated their impact on the optimisation results for ADODG benchmark Case 1. Reference [1] investigated the influence of optimisation algorithm and initial design on the optimal solution of a wing problem. Besides, Ref. [10] compared the optimised geometries obtained from several institutions using one CFD solver (i.e. Onera *elsA* software), whereas in Ref. [11], a comparison was carried out with respect to different optimisation results obtained from four well–validated CFD codes.

In this paper, the open–source suite SU2 [12, 13] is taken to perform gradient–based ASO for two aerofoil benchmark problems. The first case (i.e. ADODG Case 1) is the drag minimisation of the NACA 0012 aerofoil in transonic, inviscid flow, with a minimum thickness constraint. The second case (i.e. ADODG Case 2) is the drag minimisation of the RAE 2822 aerofoil in transonic, viscous flow, subject to lift, pitching moment and area constraints. Hicks–Henne

Bump Functions (HHBFs) and FFD are employed as geometry parameterisation method. The continuous adjoint method is used to compute the gradients.

It should be noted that the available methods for each constituent of an ASO framework have their own merits and drawbacks. Thus, the most appropriate set of methods for a specific optimisation case may not be suitable for another case. More importantly, for a given ASO framework, there are a number of parameters that affect the final optimisation result. It would require fine–tuning of those parameters in order to achieve the best optimisation performance for a specific case. To date, however, many parameters have been largely neglected in practice, and their effects on the optimal solution are therefore unknown. In this study, several key parameters are carefully selected, particularly in geometry parameterisation, which formulates the design space and provides design variables as input for optimisation. Instead of using the default (or common) value, a range of settings are specified and applied. Additionally, two sets of parameter values in turbulence modelling are used in the viscous optimisation case.

The primary aim of this paper is to establish the sensitivity of the optimal solution to a number of model parameters and to gain the "best practice" from the sensitivity assessment, which can provide suggestions of parameter settings for future aerodynamic design and optimisation. The work is built around four technical objectives. First, two parameterisation methods are used to manipulate geometry changes, and their impact on the results is investigated for two aerofoil problems. The second objective is to establish the robustness of the optimal results (from Objective 1) to changes on numerical settings used in the parameterisation methods. The third objective is to investigate the sensitivity of optimisation result to turbulence model closure coefficients in the RAE 2822 case. The last objective revisits the optimal solution with respect to design variable dimensionality, and this is carried out for both aerofoil cases.

The paper continues in Section 2 with a description of the methods and algorithms employed in this work. Then, Section 4 discusses the two ADODG benchmark problems and presents the optimisation results. Finally, conclusions

are summarised in Section 5.

2. Methodology

2.1. Optimisation Framework

The open–source suite SU2 [12, 13] has the capability to perform analysis of optimisation problems in various engineering areas. A typical design process for aerodynamic optimisation is illustrated in Figure 1. A baseline geometry and mesh are taken as input to the design cycle, along with a chosen objective function, J, to evaluate optimisation performance and a vector of design variables, $\vec{x}$, to parameterise the shape. When the gradient of the objective function, ∇J, is obtained using adjoint method, a gradient–based optimiser is then initiated to drive the design cycle and guide the search for optimum. In this work, the Sequential Least SQuares Programming (SLSQP) optimiser is used. The optimisation process is terminated when the convergence criteria, the Karush–Kuhn–Tucker (KKT) conditions [14, 15], are satisfied or the number of design iterations exceeds a maximum number.

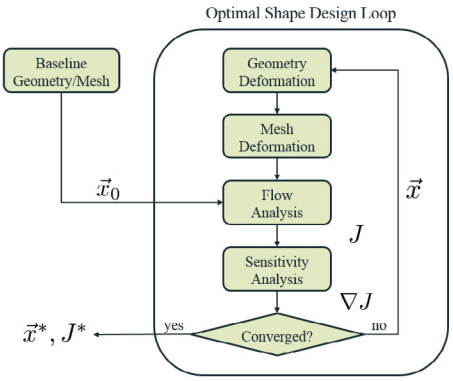

Figure 1: Flow chart for gradient–based shape optimisation within SU2.

2.2. Flow and Adjoint Solver

In this study, the flows around aerodynamic bodies are governed by compressible Euler and Reynolds–Averaged Navier–Stokes (RANS) equations. SU2

is a finite volume based CFD solver, where the Jameson–Schmidt–Turkel (JST) [16] scheme is used for spatial discretisation and the implicit Euler scheme for time marching. For RANS simulations, the Spalart–Allmaras (SA) [17] one–equation turbulence model is used to close the RANS equations. For the adjoint solver, the continuous adjoint approach is employed in this work.

2.3. Geometry Parameterisation

Two commonly–used geometry parameterisation methods are implemented in SU2, which correspond to HHBF and FFD. Both approaches are employed in this work and are discussed as follows.

2.3.1. Hicks–Henne Bump Functions

Hicks and Henne [18] introduced an analytical approach that takes a baseline geometry and adds a linear combination of bump functions to create a new shape. For two–dimensional (2D) problems, the parameterised geometry function can be expressed by:

$$\begin{cases} y = y_{\text{baseline}} + \sum_{i=1}^{n} b_i(x) \\ b_i(x) = a_i \left[\sin\left(\pi\, x^{\frac{\log 0.5}{\log h_i}} \right) \right]^{t_i}, \quad 0 \le x \le 1 \end{cases} \tag{1}$$

where n is the number of bump functions, $b_i(x)$ is the bump function (or basis function) proposed by Hicks and Henne, a_i represents the bump amplitude and acts as the weighting coefficient, h_i locates the maximum point of the bump, and t_i controls the width of the bump. By setting all of the coefficients a_i to zero, the baseline geometry is recovered.

By inspecting Eq. (1), it is apparent that the bump function, $b_i(x)$, is defined by three parameters (i.e. a_i, h_i, and t_i). The bump amplitude coefficients, a_i, are treated as design variables and can be varied during optimisation, while the other two parameters, h_i and t_i, are predetermined and fixed in optimisation.

With respect to the locations of bump peak, h_i, two distribution approaches are employed in this study: a) uniform distribution along the aerofoil chord–wise direction; and b) uneven distribution described by a "one–minus–cosine"

function:

$$h_i = \frac{1}{2}\left[1 - \cos\left(\frac{i\,\pi}{n+1}\right)\right], \quad i = 1, \ldots, n. \tag{2}$$

A comparison of these two distribution approaches is illustrated in Figure 2, where a set of bump functions are imposed on the NACA 0012 aerofoil. It is worth noting that the "one–minus–cosine" distribution provides a better clustering of design variables at the leading and trailing–edge of the aerofoil when compared with the uniform distribution.

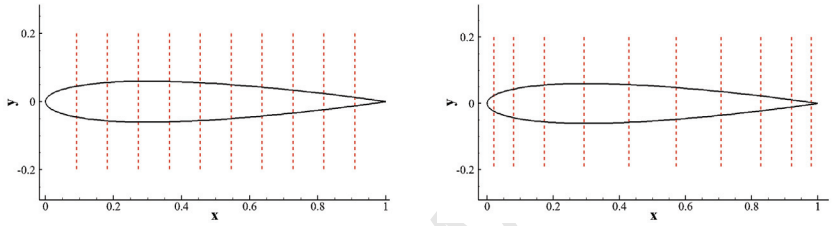

(a) Uniform distribution (b) "One–minus–cosine" distribution

Figure 2: Illustration of two distribution approaches for HHBFs ($n = 10$) on the NACA 0012 aerofoil. Red dashed lines indicate locations of bump peak.

Regarding the bump width control parameter, t_i, a constant value is specified for all bump functions within SU2. In this study, in addition to the default setting $t = 3$, a range of integer values are defined, and their impact on the optimisation result is investigated. Figure 3 shows three sets of HHBFs with different settings of t. It is observed that the bump width narrows down as t increases, which suggests that a relatively smaller value of t can provide more global shape control whereas a relatively larger value of t generates more local shape control.

2.3.2. Free–Form Deformation

Free–Form Deformation (FFD), initially proposed by Sederberg and Parry [19], is used as the second parameterisation method in this work. The basic FFD concept can be visualised as embedding a flexible object inside a flexible volume and deforming both of them simultaneously by perturbing the lattice of

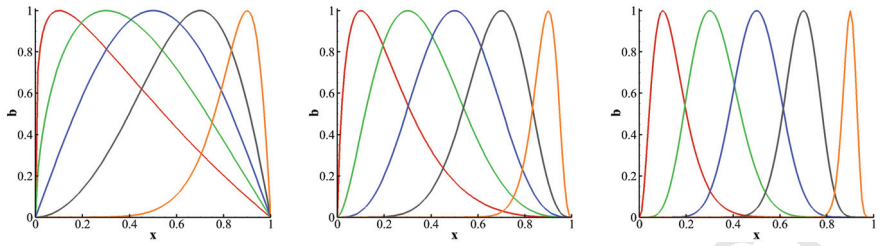

(a) $t = 1$ (b) $t = 3$ (default) (c) $t = 10$

Figure 3: Three sets of HHBFs ($n = 5$, $a_i = 1$, and uniformly distributed in the range of $h_i \in [0.1, 0.9]$) with different value settings of bump width control parameter.

the volume. The FFD control volume (or FFD box) usually has a topology of a cube when deforming three–dimensional (3D) objects or a rectangle for 2D geometries, and thus can be parameterised as either a trivariate volume or a bivariate surface. In this study, Bézier curve is used as the FFD blending function. Figure 4 illustrates the FFD box encapsulating a rectangular wing and the RAE 2822 aerofoil, where a lattice of control points are uniformly spaced on the surface of FFD box.

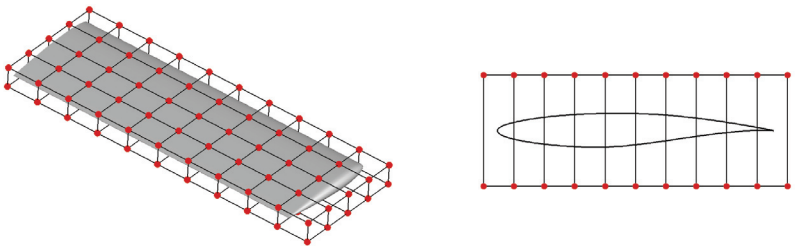

(a) 3D rectangular wing (b) 2D RAE 2822 aerofoil

Figure 4: View of FFD box enclosing the embedded object, including the control points shown as red spheres.

The parameterised Bézier volume can be described using the following equation:

$$\mathbf{X}(\xi, \eta, \zeta) = \sum_{i=0}^{l} \sum_{j=0}^{m} \sum_{k=0}^{n} \mathbf{P}_{i,j,k} B_i^l(\xi) B_j^m(\eta) B_k^n(\zeta) \tag{3}$$

where l, m, n are the degrees of FFD blending function; ξ, η, $\zeta \in [0, 1]$ are the parametric coordinates; $\mathbf{P}_{i,j,k}$ are the Cartesian coordinates of the control point (i, j, k); $\mathbf{X}$ are the corresponding Cartesian coordinates (x, y, z) for a given (ξ, η, ζ) in the Bézier volume; $B_i^l(\xi)$, $B_j^m(\eta)$, and $B_k^n(\zeta)$ are the Bernstein polynomials, which are expressed as

$$\begin{cases} B_i^l(\xi) = \dfrac{l!}{i!\,(l-i)!}\,\xi^i\,(1-\xi)^{l-i} \\ B_j^m(\eta) = \dfrac{m!}{j!\,(m-j)!}\,\eta^j\,(1-\eta)^{m-j} \\ B_k^n(\zeta) = \dfrac{n!}{k!\,(n-k)!}\,\zeta^k\,(1-\zeta)^{n-k} \end{cases} \tag{4}$$

The control points of the FFD box are defined as the design variables, the number of which depends on the degree of the chosen Bernstein polynomials. It should be noted that these control points are uniformly spaced in the FFD domain otherwise the initial geometry of the embedded object can not be recovered with the original positions of the control points.

FFD is numerically executed in three steps. Firstly, for the embedded object, a mapping is performed from the physical space to the parametric space of the FFD box. The parametric coordinates (ξ, η, ζ) of each surface mesh node are determined and remain unchanged during optimisation. Note that this mapping is evaluated only once. Secondly, the FFD control points are perturbed, which leads to the deformation of the FFD box as well as the embedded object. Thirdly, once the FFD box is deformed, the new Cartesian coordinates (x, y, z) of the embedded object in the physical space are algebraically computed using Eq. (3).

Because the position settings of the FFD box are subject to the users' choice and may affect the final optimisation result, the impact of FFD box position on the optimisation performance is thus investigated in this study.

2.4. Mesh Deformation

Once the geometry is perturbed with a chosen parameterisation, the surrounding volume mesh needs to be deformed. The technique employed in SU2

models the computational mesh as an elastic solid using the equations of linear elasticity [20]. In this study, the modulus of elasticity for each mesh cell is treated to be inversely proportional to the cell volume, which can preserve the mesh quality in boundary layers and regions of high resolution.

2.5. Gradient Evaluation

The gradient evaluation within SU2 framework can be formulated as the following equation:

$$\underbrace{\begin{bmatrix} \frac{\partial f}{\partial x_1} \\ \frac{\partial f}{\partial x_2} \\ \vdots \\ \frac{\partial f}{\partial x_n} \end{bmatrix}}_{\text{Gradients}} = \underbrace{\begin{bmatrix} \frac{\partial s_1}{\partial x_1} & \cdots & \frac{\partial s_m}{\partial x_1} \\ \vdots & \ddots & \vdots \\ \frac{\partial s_1}{\partial x_n} & \cdots & \frac{\partial s_m}{\partial x_n} \end{bmatrix}}_{\text{Geometric Sensitivities}} \underbrace{\begin{bmatrix} \frac{\partial f}{\partial s_1} \\ \frac{\partial f}{\partial s_2} \\ \vdots \\ \frac{\partial f}{\partial s_m} \end{bmatrix}}_{\text{Surface Sensitivities}} \tag{5}$$

where n and m are the number of design variables and surface mesh nodes, respectively; f represents the function of interest, being the objective or constraint function; x_i ($i = 1, 2, \ldots, n$) are the design variables; the variables s_j ($j = 1, 2, \ldots, m$) represent the local surface normal displacements for each discrete mesh node on the geometry surface.

The term $\partial f/\partial \mathbf{s}$ is called surface sensitivities, which represent the variation of the function of interest with respect to infinitesimal perturbations of the geometry shape in local surface normal direction. The surface sensitivities at each mesh node are computed by solving only once the adjoint equations, of which the computational cost is similar to that of one flow solution. The Jacobian matrix $\partial \mathbf{s}/\partial \mathbf{x}$ is known as geometric sensitivities, which measure the influence of the change of design variables on the positions of surface mesh nodes. The geometric sensitivities are calculated using finite difference method, of which the computational cost is negligible as it does not involve the solution of governing equations. The gradients $\partial f/\partial \mathbf{x}$ are then computed through a dot product operation between the geometric and surface sensitivities. The computational cost of evaluating gradients using the adjoint method is virtually independent of the

number of design variables, which provides great efficiency for gradient–based optimisation problems.

2.6. Summary

A summary of the computational methods and numerical settings used in this study is given in Table 1.

Table 1: Computational methods and numerical settings for the ADODG benchmark cases.

ADODG	Case 1: NACA 0012	Case 2: RAE 2822
Geometry parameterisation	HHBF/FFD	HHBF/FFD
Mesh deformation	Linear elasticity equations	Linear elasticity equations
Flow governing equations	Euler	RANS
Turbulence model	–	SA
Spatial discretisation	JST	JST
Time discretisation	Euler implicit	Euler implicit
Optimiser	SLSQP	SLSQP
Gradient evaluation	Continuous adjoint	Continuous adjoint
Maximum number of iterations	100	100
Tolerance of KKT conditions	$1 \cdot 10^{-6}$	$1 \cdot 10^{-6}$

3. Test Cases Description

Two aerofoil optimisation cases defined by ADODG were selected for investigation. This section contains the case description, problem formulation as well as computational mesh.

3.1. ADODG Case 1

3.1.1. Problem Description

The optimisation problem is the drag minimisation of a modified NACA 0012 aerofoil in inviscid, transonic flow. The freestream Mach number, M, is 0.85, and the angle of attack, α, is fixed at 0 degree. The thickness is constrained to

be greater than or equal to that of the initial aerofoil along the entire chord. The optimisation problem is written as

$$\begin{aligned} \text{Minimise:} \quad & C_d \\ \text{Subject to:} \quad & y(x) \geq y_{baseline}(x), \forall\, x \in [0,\, 1] \end{aligned}$$

where C_d is the drag coefficient, x is the coordinate along the aerofoil chord, and y is the coordinate describing the thickness of the symmetric aerofoil.

3.1.2. Computational Mesh

As the flow is symmetric around the aerofoil at the prescribed flow conditions, only the upper aerofoil surface is modelled unless otherwise stated. The structured O–grid is used for this case and is shown in Figure 5. A preliminary grid convergence study was performed, and the coarse mesh was found adequate, which has 129 points in the circumferential direction and 65 in the normal direction. An inviscid flow analysis was carried out on the baseline aerofoil and the drag coefficient was evaluated at 468.02 counts (1 count = 10^{-4}).

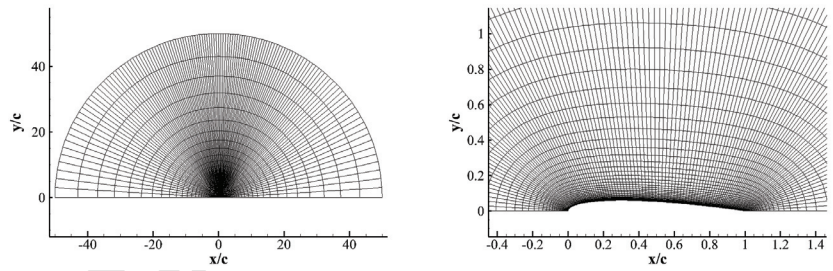

(a) Far view (b) Near view

Figure 5: Case 1: computational domain and coarse mesh (129 × 65) for the NACA 0012 aerofoil.

3.2. ADODG Case 2

3.2.1. Problem Description

The second optimisation problem is the drag minimisation of the RAE 2822 aerofoil in viscous, transonic flow. The freestream Mach number is 0.734, and

the Reynolds number, Re, is $6.5 \cdot 10^6$. The lift coefficient is constrained to 0.824, the pitching moment coefficient (evaluated at the quarter–chord) must be no less than -0.092, and the aerofoil area must be greater than or equal to the initial aerofoil area during the optimisation process. The optimisation problem is written as

$$\begin{aligned} \text{Minimise:} \quad & C_d \\ \text{Subject to:} \quad & C_l = 0.824 \\ & C_m \geq -0.092 \\ & S \geq S_0 \end{aligned}$$

where C_d, C_l and C_m are the drag, lift, and pitching moment coefficients, respectively; and S and S_0 are the optimised and initial aerofoil areas, respectively. In order to satisfy the lift constraint, the angle of attack is set up as an additional design variable in this optimisation case.

3.2.2. Computational Mesh

As shown in Figure 6, the structured C–grid is used for the RAE 2822 case. The coarse mesh consists of 385×65 grid points in the wrap–around and normal directions respectively, where 257 points are distributed along the aerofoil and 65 points in the grid cut. The first grid line of the wall was placed at $1 \cdot 10^{-5}$ (for a chord of 1) to ensure that the y^+ is below 1. From preliminary study, the coarse mesh was found adequate to guarantee mesh independent solutions and was thus used for this case.

For the initial aerofoil, the compressible RANS simulation was carried out using the standard single–equation SA turbulence model. Note that the angle of attack was iteratively updated during the flow analysis in order to meet the lift target. It was found that $C_d = 241.24$ counts, $S_0 = 0.07787$, and $C_m = -0.089$.

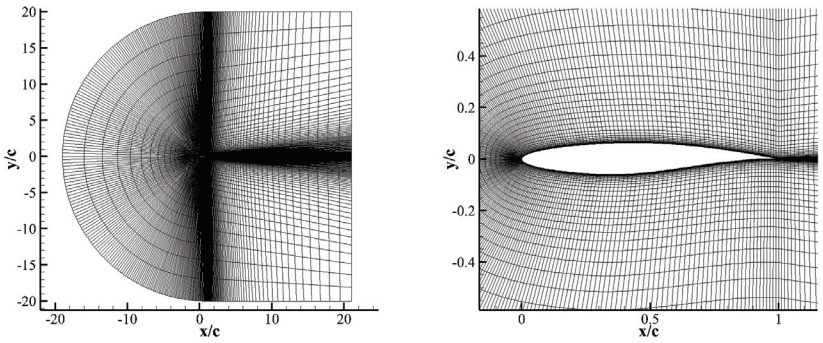

(a) Far view (b) Near view

Figure 6: Case 2: computational domain and coarse mesh (385 × 65) for the RAE 2822 aerofoil.

4. Results

This section contains optimisation results obtained from two benchmark problems. This work particularly focuses on investigating the sensitivity of the optimal solution to a series of model parameters, with the purpose of finding a suite of parameter values that can produce the best optimisation result.

Prior to optimisation, a number of parameter values need to be determined, particularly in geometry parameterisation. The HHBF has two coefficients that need to be specified. For locations of bump peak, h_i, two distribution approaches are employed. For bump width control coefficient, t, a range of integer values are used. In terms of FFD, various settings of FFD box position are defined. Additionally, the number of design variables, n_{dv}, is varied within a reasonable range to perform the dimensionality study. For the RAE 2822 case, two sets of closure coefficients of SA turbulence model are used. The main numerical parameters used in the test cases are summarised in Table 2.

Table 2: Numerical parameters for the ADODG benchmark cases; the values in square brackets indicate the range for specific parameter.

ADODG	Case 1: NACA 0012	Case 2: RAE 2822
HHBF		
Distribution approach	Uniform/One–minus–cosine	Uniform/One–minus–cosine
Bump width control parameter	[1, 15]	[1, 10]
Number of design variables	[5, 40]	[5, 40]
FFD		
FFD box: upper/lower	[±0.0601, ±0.3]	[±0.08, ±0.4]
FFD box: left	[-0.01, -0.0001]	[-0.01, -0.0001]
FFD box: right	[1.0001, 1.01]	[1.0001, 1.01]
Number of design variables	[5, 40]	[5, 40]
Turbulence model	–	Standard SA/Calibrated SA

4.1. ADODG Case 1

4.1.1. Impact of Parameter Settings in Hicks–Henne Bump Functions

The design variables (i.e. bump amplitude coefficients a_i) are restricted to have non–negative values in this case. Consequently, the deformed aerofoil is guaranteed to have a larger thickness along the chord than the initial aerofoil. Therefore, the constrained optimisation problem is transformed to an unconstrained one by satisfying the thickness constraint implicitly. Optimisations were carried out using the parameter settings in Table 2. A 3D carpet plot of drag coefficient versus n_{dv} and t for both uniform and "one–minus–cosine" distributions can be obtained. Some sections are extracted from the 3D plot, and the corresponding optimisation results are shown and discussed as follows.

By applying two HHBF distribution approaches, the final drag results are plotted versus the number of design variables in Figure 7(a). Note that the presented results correspond to the setting of $t = 8$. With respect to other values of t, the results show a similar pattern and are not reported herein for brevity. It is apparent that the "one–minus–cosine" distribution outperforms the uniform

distribution by producing significantly lower drag values, suggesting a large dependence of the optimal solution on the distribution of the bump functions. As shown later, the geometry shape deformations are mainly concentrated in the fore and aft section of the aerofoil, indicating that the "one–minus–cosine" distribution is preferably used in the NACA 0012 optimisation case.

The exception only occurs at $n_{dv} = 5$, where the uniform distribution method performs better. It was found that the optimised geometry exhibits a flatter aft section when using the uniform distribution and a weaker shock is generated. Nonetheless, the number of design variables in this case is too small to fully cover the design space. This exception is thus not representative of the overall trend.

As the number of design variables is increased, the drag coefficient exhibits a convergence feature, especially for "one–minus–cosine" distribution, which suggests the design space is gradually explored. Moreover, the gap between these two groups of drag values becomes smaller when using more design variables. The drag difference is 39.1 counts for the case of $n_{dv} = 40$, and the difference is further decreased to 21.6 counts as n_{dv} is doubled from 40 to 80. In the context hereafter, the "one–minus–cosine" distribution approach is used for the NACA 0012 aerofoil optimisation case.

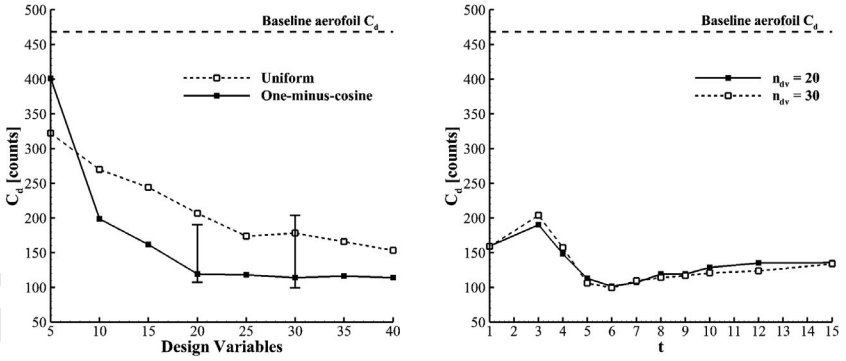

(a) Bump function distribution ($t = 8$) (b) Bump width control parameter

Figure 7: Case 1: influence of HHBF parameters on drag coefficient ($M = 0.85$, $\alpha = 0$ deg).

With respect to $n_{dv} = 20$ and $n_{dv} = 30$, Figure 7(b) shows the final drag results plotted versus the bump width control parameter. An evident observation is that the drag value drops sharply when t is increased from 3 to 5. Regarding the optimisation performance, the results obtained from $t = 3$ and $t = 6$ correspond to the two ends of the spectrum (shown as error bars in Figure 7(a)), where the drag difference for $n_{dv} = 30$ is over 100 counts. This indicates that the bump width control parameter also has a large impact on the optimal solution in this optimisation case.

To find out the cause for this fact, three representative groups of optimisation results are compared in Figure 8. An evident distinction is observed in the leading edge area of the optimised aerofoil shape: a significantly blunt leading edge is generated with setting of $t = 6$ or $t = 10$, whereas the surface perturbation is trivial for the setting of $t = 3$. As mentioned earlier, when the bump width control parameter t is set up with a larger value, more local shape control is achieved in geometry parameterisation. This property accounts for the fact that the setting of $t = 6$ or $t = 10$ effectively deforms the aerofoil in the narrow region near the leading edge, while the setting of $t = 3$ did not exhibit the same behaviour. Consequently, a suction peak in the pressure coefficient distribution is generated for $t = 6$ and $t = 10$, whereas the C_p distribution for $t = 3$ remains almost unchanged from the baseline aerofoil near the leading edge. Due to the existence of pressure recovery after the suction peak, the two cases with larger values of t exhibit a weaker shock near the trailing edge and thus generate a lower wave drag. Since the wave drag contributes most to the total drag in this optimisation problem, it is not unexpected that the two larger values of t result in much better optimisation performance than that of $t = 3$. With consideration of the fact that $t = 6$ produces the lowest drag among all settings, this value is used hereafter for the NACA 0012 aerofoil optimisation case.

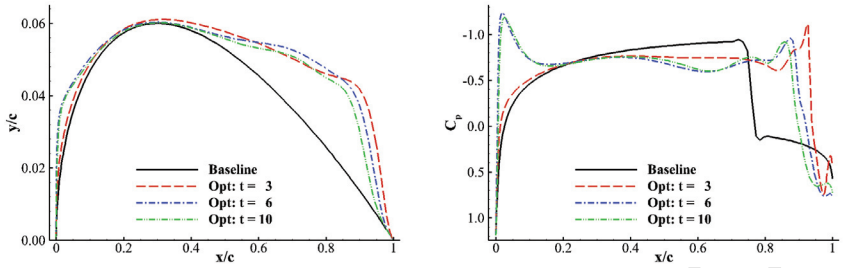

(a) Aerofoil shape (b) Pressure coefficient distribution

Figure 8: Case 1: influence of Hicks–Henne bump width control parameter on optimisation results ($n_{dv} = 30$, $M = 0.85$, and $\alpha = 0$ deg).

4.1.2. Impact of Parameter Settings in Free–Form Deformation

Two FFD parameterisation approaches embedded in SU2 framework are used in the NACA 0012 optimisation case, which are FFD control point and FFD thickness method. An example of the commonly–used FFD control point parameterisation is demonstrated in Figure 9(a). The design variables are specified for the control points on the upper surface of FFD box, whereas the control points on the lower surface are held fixed during optimisation because only the upper half aerofoil geometry is used. Due to the symmetric characteristic of the flowfield, the FFD thickness approach is also employed for this optimisation problem, which is illustrated in Figure 9(b). In this approach, the whole aerofoil geometry as well as corresponding computational mesh are used. The thickness at specific chord–wise position of the aerofoil can be modified by manipulating a pair of control points, which move with the same magnitude but in opposite directions. For both FFD methods, the thickness constraint in this optimisation problem can be satisfied implicitly by allowing the control points to move only in the outward direction as shown in Figure 9.

The FFD box has a rectangular shape in this case and is defined by four boundaries. Optimisation can be successfully performed as long as these boundaries do not intersect with the embedded geometry and are located not too far from the aerofoil. Nonetheless, it was found that the drag result for the opti-

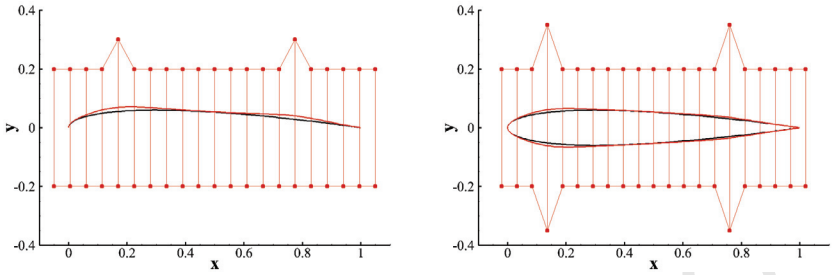

(a) FFD control point method (b) FFD thickness method

Figure 9: Case 1: two FFD parameterisation approaches for the NACA 0012 aerofoil optimisation case. Baseline aerofoil is shown in black colour and deformed aerofoil in red.

mised aerofoil has a dependence on different settings of the FFD box position. A combination of the four boundary positions that can produce the best optimisation performance are listed in Table 3, and these FFD box settings are used hereafter for the NACA 0012 aerofoil optimisation case.

Table 3: Case 1: settings of FFD box position with best practice for the NACA 0012 aerofoil optimisation case.

Parameterisation Method	B_{upper}	B_{lower}	B_{left}	B_{right}
FFD control point	$y = 0.2000$	$y = -0.2000$	$x = -0.0010$	$x = 1.0010$
FFD thickness	$y = 0.0601$	$y = -0.0601$	$x = -0.0001$	$x = 1.0001$

4.1.3. Dimensionality Study

The dimensionality study was conducted using the best practice obtained from above investigation. Figure 10 plots the aerofoil shapes and C_p distributions for the optimised designs using HHBF parameterisation approach. As more design variables are used, the leading edge becomes blunter and the aft section of the aerofoil gets thicker, indicating that a flatter aerofoil surface is created. Correspondingly, a suction peak is generated in the C_p distribution near the leading edge and becomes steeper as n_{dv} is increased. The shock position moves further downstream towards the trailing edge.

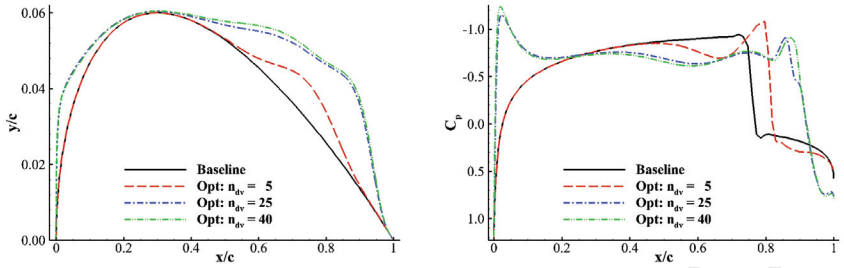

(a) Aerofoil shape (b) Pressure coefficient distribution

Figure 10: Case 1: influence of design variable dimensionality on optimisation results using HHBF approach ($M = 0.85$, $\alpha = 0$ deg).

Figure 11 displays FFD box perturbation and aerofoil deformation using FFD thickness parameterisation method. As more control points are placed on the surface of FFD box, the optimiser is provided with more freedom to explore the design space, and thus better optimisation results are obtained.

The final drag results of the dimensionality study are shown in Figure 12. For both FFD methods, the drag coefficient monotonically decreases as more design variables are added into optimisation; for HHBF approach, however, the drag value initially drops sharply and then maintains a nearly constant level. This indicates that around 15 Hicks–Henne design variables are sufficient to cover the design space, while more FFD design variables are needed to do so. This fact is possibly caused by the difference of design variable distribution. The bump functions are distributed using "one–minus–cosine" function and are clustered in the area where the surface sensitivities are relatively large. By contrast, the control points are placed uniformly on the surface of FFD box, which means that more design variables are needed for the optimiser to fully explore the design space. In terms of optimisation performance, approximately 80% of drag reduction is achieved with the best result for each parameterisation method. Specifically, FFD control point method produces the lowest drag with 80.5 counts in the optimisation case using 40 design variables, which corresponds to 82.8% of drag reduction.

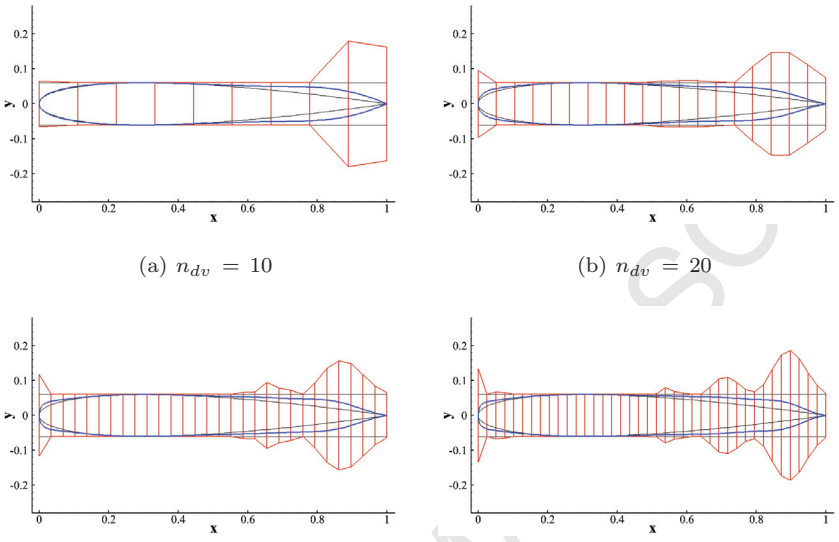

(a) $n_{dv} = 10$ (b) $n_{dv} = 20$

(c) $n_{dv} = 30$ (d) $n_{dv} = 40$

Figure 11: Case 1: FFD box perturbation and geometry deformation for dimensionality study using FFD thickness parameterisation method (original FFD box and aerofoil geometry in black, deformed FFD box in red and deformed aerofoil geometry in blue).

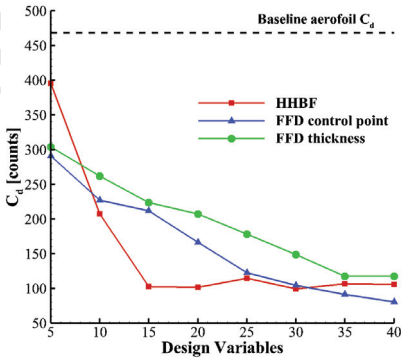

Figure 12: Case 1: drag coefficient results obtained from dimensionality study using three parameterisation methods ($M = 0.85$, $\alpha = 0$ deg).

For the case with 40 design variables, the optimised aerofoil shapes and pressure coefficient distributions are compared in Figure 13 with respect to three parameterisation methods. It is worth observing that very similar optimisation results are obtained, reflecting that the parameterisation methods employed in this work are equivalently effective for this optimisation problem.

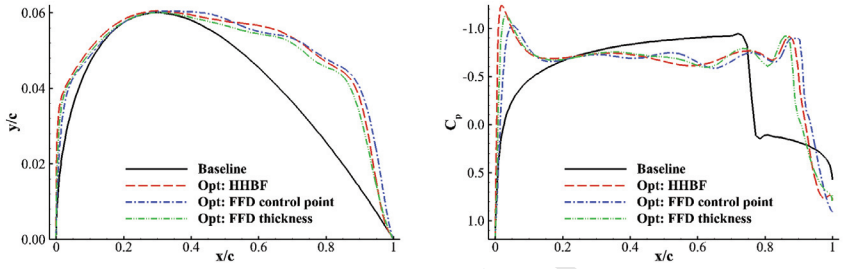

(a) Aerofoil shape (b) Pressure coefficient distribution

Figure 13: Case 1: comparison of optimisation results obtained from using three parameterisation methods ($n_{dv} = 40$, $M = 0.85$, and $\alpha = 0$ deg).

4.1.4. Optimisation Result Analysis

The drag reduction mechanism in this optimisation problem is to minimise the strength of the shock wave. A representative optimisation case with 30 Hicks–Henne design variables is taken for analysis. Figure 14 displays the Mach contours for both the baseline and optimised aerofoil. A rather flat aerofoil surface is created by the optimiser through thickening the leading edge as well as the aft section. For the baseline aerofoil, a strong shock exists at about three quarter–chord position, whereas for the optimised aerofoil, the shock is substantially weakened and is pushed further downstream, locating at around 90% chord–wise position. Hence, the total drag is substantially reduced by minimising the wave drag.

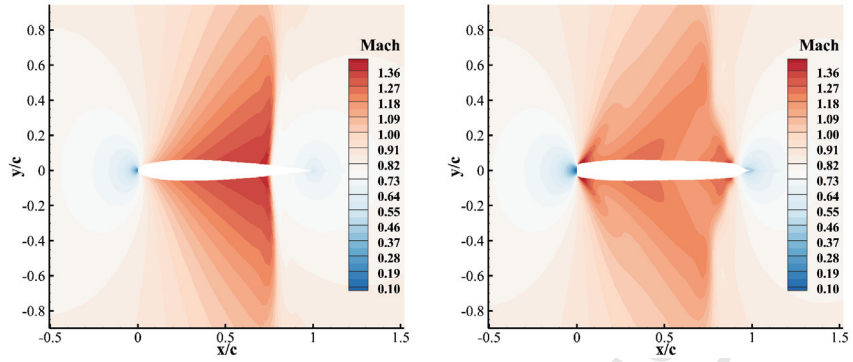

(a) Baseline aerofoil (b) Optimised aerofoil

Figure 14: Case 1: Mach contours for baseline and optimised NACA 0012 aerofoil using HHBF parameterisation method ($n_{dv} = 30$, $M = 0.85$, and $\alpha = 0$ deg).

4.2. ADODG Case 2

4.2.1. Impact of Parameter Settings in Geometry Parameterisation

Both the HHBF and FFD control point approach are employed for geometry parameterisation. The impact of parameter settings on optimisation performance is firstly investigated. The final drag results are shown in Figure 15. It is apparent that the same level of optimisation performance is achieved using different parameter settings, which implies that the optimal solution in this case is insensitive to the settings of both bump function distribution and bump width control parameter. In this study hereafter, the uniform distribution is selected and the setting of $t = 3$ is used. With respect to FFD parameterisation, the optimisation performance also shows independence of FFD box position, and the results are not reported herein for brevity.

4.2.2. Dimensionality Study

The effect of dimensionality on the optimal solution is then investigated, and the final drag results are shown in Figure 16. It is observed that the drag values vary in a very small range and the optimisation performance does not improve when using more design variables. The design space is easily explored in this case as only 5 design variables are required to locate the optimum. Additionally,

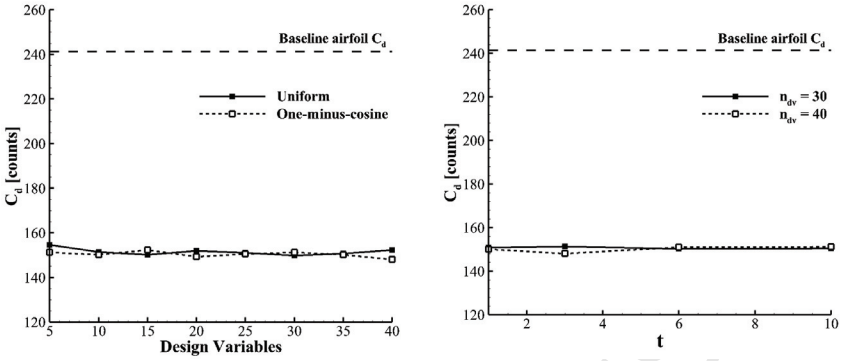

(a) Bump function distribution ($t = 3$) (b) Bump width control parameter

Figure 15: Case 2: influence of HHBF parameters on drag coefficient ($M = 0.734$, $C_l = 0.824$, and $Re = 6.5 \cdot 10^6$).

HHBF and FFD control point methods are found to be equivalently effective for this optimisation problem, achieving approximately 38% of drag reduction in both cases.

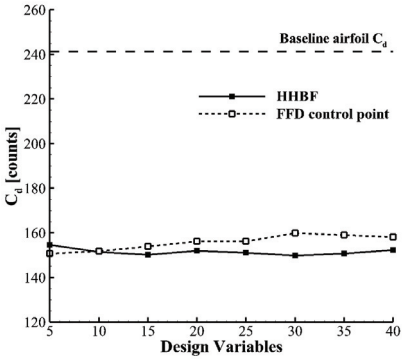

Figure 16: Case 2: drag coefficient results obtained from dimensionality study using two parameterisation methods ($M = 0.734$, $C_l = 0.824$, and $Re = 6.5 \cdot 10^6$).

4.2.3. Sensitivity of Turbulence Model Closure Coefficients

For the RAE 2822 aerofoil, the solution of the RANS equations employs the SA turbulence model, and the closure coefficients are set to standard values. However, there is no guarantee that standard values are universal for all test

cases. Da Ronch *et al.* [21] recently revisited the calibration of the SA closure coefficients for the RAE 2822 aerofoil in transonic flow. The calibration was performed with the aid of machine learning and adaptive design of experiment techniques by minimising the deviation of numerical C_p results from available experimental data. Both standard and calibrated values of SA closure coefficients are listed in Table 4. It is worth noting that the last five parameters (c_{w2} through c_{t4}) were kept at their nominal values in the case tested as they have nearly zero influence on the outputs. The reader is referred to Ref. [21] for more details about the calibration process.

Table 4: Case 2: standard and calibrated values of SA turbulence model closure coefficients. [21]

Parameter	Standard value	Calibrated value
k	0.4100	0.3600
c_{v1}	7.1000	7.5000
σ	0.6667	1.0030
c_{b1}	0.1355	0.1400
c_{w2}	0.3000	0.3000
c_{b2}	0.6220	0.6220
c_{t3}	1.2000	1.2000
c_{w3}	2.0000	2.0000
c_{t4}	0.5000	0.5000

The above two sets of parameter values for SA turbulence model were employed in the RAE 2822 optimisation case. The HHBF was used as the parameterisation approach. Since the design space is easily explored in this case, the number of Hicks–Henne design variables ranges from 5 to 10 herein. Optimisations were then carried out using both standard and calibrated SA models, and the corresponding drag results are shown in Figure 17.

For the baseline RAE 2822 aerofoil, it is observed from Figure 17(a) that the drag results obtained from using standard and calibrated SA model differ

by approximately 15 counts, which is close to the value reported in Ref. [21]. This is indicative of a certain sensitivity of the RANS solution on the SA turbulence model coefficients. Figure 18 shows the difference in the flowfield solutions obtained using the standard and calibrated SA model. The differences mainly exist at the shock region. The reason is attributed to the fact that the C_p distribution with calibrated SA model improves the agreement with the experimental data, particularly near the leading edge and at the shock front.

For the optimised RAE 2822 aerofoil, the drag results obtained when using calibrated SA model are, on average, 12 counts lower than those obtained when using the standard model. As shown in Figure 17(b), the drag reduction is, on average, 1.1% higher when replacing standard SA model by calibrated model. In the area of aircraft design, a high level of accuracy with respect to drag prediction is required, and this need is confirmed by Meredith [22], who showed that one drag count is equal to the weight of one passenger in a long–haul aircraft. This highlights the importance of turbulence modelling, and the need for more extensive calibration campaigns to reduce modelling uncertainties. A further dependence of the optimal solution would be on the turbulence model, which is not done in this work, but the reader may have an indication of its importance by looking at other references [23, 24].

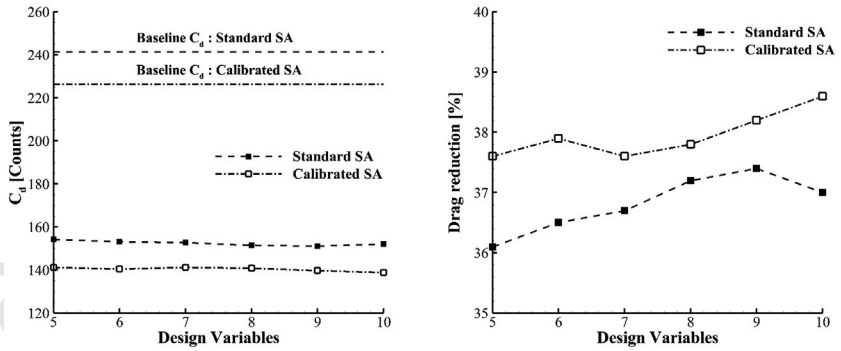

(a) Drag coefficient values (b) Percentage of drag reduction

Figure 17: Case 2: comparison of drag results obtained from optimisation using two sets of SA turbulence model closure coefficients ($M = 0.734$, $C_l = 0.824$ and $Re = 6.5 \cdot 10^6$).

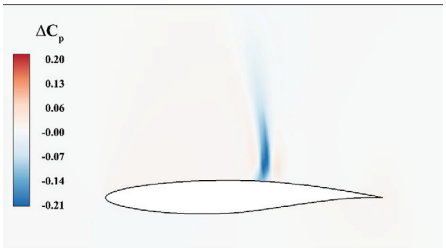

Figure 18: Case 2: difference of pressure coefficient in baseline RAE 2822 flowfield solutions obtained using standard and calibrated SA turbulence models ($M = 0.734$, $C_l = 0.824$ and $Re = 6.5 \cdot 10^6$).

4.2.4. Optimisation Result Analysis

The optimisation case selected for analysis has 20 Hicks–Henne design variables and uses standard SA turbulence model. For both the baseline and optimised design, the Mach contour results are shown in Figure 19. The strong shock wave on the upper surface of the baseline aerofoil is eliminated after optimisation. Thus, the total drag is reduced by removing the component of wave drag. In order to further understand the drag reduction mechanism, the aerofoil shapes, C_p distributions as well as surface curvature distributions are plotted in Figure 20 for comparison. The geometry deformation largely occurs in the fore section of the aerofoil. On the upper side, the curvature is reduced to create a relatively flat surface, which alleviates the flow acceleration and hence delays or eliminates the formulation of shock wave; whereas on the lower side, the aerofoil becomes thicker, which is primarily to satisfy the area constraint. Correspondingly, the pressure discontinuity at around 56% chord–wise position is replaced by a smooth pressure recovery, thus eliminating the shock wave and reducing the drag. Additionally, the surface curvature near the trailing edge is enlarged after optimisation, and the local camber is increased accordingly.

We have further investigated the impact that the optimal shape has on the aerodynamic derivatives. Results are summarised in Table 5. It was found that the influence on the drag and pitching moment curve slopes, $dC_d/d\alpha$ and $dC_m/d\alpha$ respectively, is minimal but significant on the lift curve slope, $dC_l/d\alpha$.

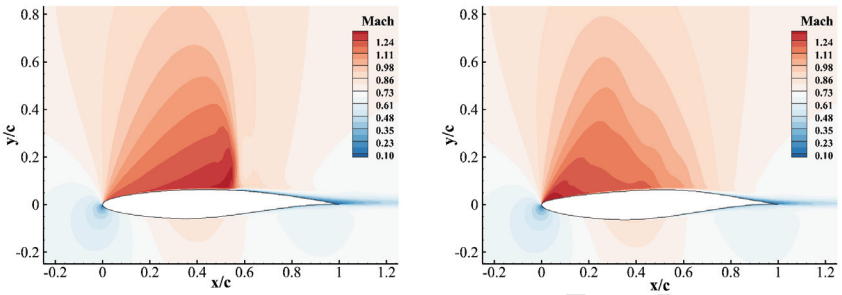

(a) Baseline aerofoil (b) Optimised aerofoil

Figure 19: Case 2: Mach contours for baseline and optimised RAE 2822 aerofoil using HHBF parameterisation method ($M = 0.734$, $C_l = 0.824$, $Re = 6.5 \cdot 10^6$, and $n_{dv} = 20$).

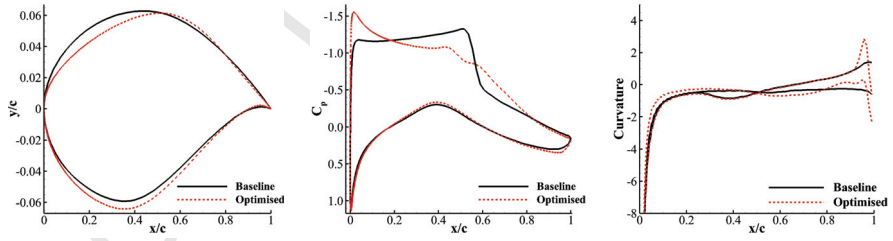

(a) Aerofoil shape (b) Pressure coefficient distribution (c) Surface curvature

Figure 20: Case 2: comparison of optimisation results for the RAE 2822 aerofoil optimisation using HHBF parameterisation method ($M = 0.734$, $C_l = 0.824$, $Re = 6.5 \cdot 10^6$, and $n_{dv} = 20$).

This may potentially affect the aerodynamic response to gusts.

Table 5: Case 2: aerodynamic derivatives of the RAE 2822 aerofoil at the design point ($M = 0.734$, $C_l = 0.824$, $Re = 6.5 \cdot 10^6$, and $n_{dv} = 20$).

	$dC_l/d\alpha$	$dC_d/d\alpha$	$dC_m/d\alpha$
Baseline	0.0806	0.01500	0.0022
Optimal	0.1241	0.01474	0.0021

For this optimisation case, the convergence histories of several constraints are plotted in Figure 21. Firstly, the lift coefficient initially deviates from the value of 0.824 because the shape deformation is mainly performed in the first few design steps. The lift coefficient then gradually recovers to the target value and finally satisfies the constraint. Secondly, despite an initial decrease of the pitching moment coefficient, the optimisation seeks to generate aerofoils with higher C_m values in the following design cycles, which leaves more margin for this constraint. Thirdly, the aerofoil area basically remains the same value throughout the optimisation process, and hence does not violate the area constraint. Therefore, the optimisation provides a feasible design that meets the requirement of this benchmark problem.

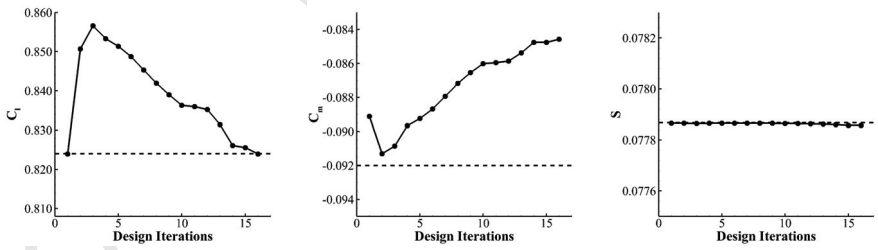

(a) Lift (b) Pitching moment (c) Surface area

Figure 21: Case 2: convergence histories of several constraints in the RAE 2822 optimisation using HHBF parameterisation method ($n_{dv} = 20$). Dashed line indicates the desired value for a specific constraint.

5. Conclusions

This work focused on investigating the sensitivity of the optimal solution to numerical parameters which have been neglected to date. The open–source suite, SU2, was applied to perform gradient–based aerodynamic optimisation using continuous adjoint method. Two aerofoil benchmark problems were exercised, and in both transonic cases, the drag was minimised by either weakening or eliminating the shock.

Several conclusions may be formulated from this study. Firstly, Hicks–Henne bump functions and free–form deformation were shown to be equivalently effective as geometry parameterisation method for both optimisation problems. Secondly, the optimisation of the NACA 0012 aerofoil exhibits strong dependence on virtually all numerical parameters investigated. This dependence reflects the high curvature seen locally on the optimised shape. Fine–tuning of these parameters is thus required to provide sufficient local shape control. Thirdly, in the RAE 2822 case, the insensitivity of optimisation results to numerical parameters arises from low to mild curvatures on the final shape. The design space is easily explored by perturbing moderately the geometry. Lastly, the optimisation performance is influenced by turbulence modelling as the RANS solution shows a certain sensitivity to the closure coefficients of Spalart–Allmaras turbulence model. A good calibration of the turbulence model is thus needed.

Overall, there is no a priori knowledge that we can use to know the degree of sensitivity of the optimal design to numerical settings. This can only be estimated a posteriori by running a number of analyses. The sensitivity study conducted for the two aerofoil cases may provide guidance for complex optimisation problems.

Acknowledgements

The authors acknowledge the financial support from the Engineering and Physical Sciences Research Council (grant number: EP/P006795/1) and the use of the IRIDIS High Performance Computing Facility, and associated support

services at the University of Southampton, in the completion of this work. Yang also acknowledges the financial support from China Scholarship Council (CSC) and the University of Southampton.

Data supporting this study are openly available from the University of Southampton repository at `https://doi.org/10.5258/SOTON/D0625`.

References

[1] Y. Yu, Z. Lyu, Z. Xu, J. R. Martins, On the influence of optimization algorithm and initial design on wing aerodynamic shape optimization, Aerospace Science and Technology 75 (2018) 183–199.

[2] C. Lee, D. Koo, D. W. Zingg, Comparison of B-spline surface and free-form deformation geometry control for aerodynamic optimization, AIAA Journal 55 (1) (2016) 228–240.

[3] G. Carrier, D. Destarac, A. Dumont, M. Meheut, I. Salah El Din, J. Peter, S. Ben Khelil, J. Brezillon, M. Pestana, Gradient-based aerodynamic optimization with the elsA software, in: 52nd Aerospace Sciences Meeting, 2014, p. 0568.

[4] J. Fincham, M. Friswell, Aerodynamic optimisation of a camber morphing aerofoil, Aerospace Science and technology 43 (2015) 245–255.

[5] A. Morris, C. Allen, T. Rendall, CFD-based optimization of aerofoils using radial basis functions for domain element parameterization and mesh deformation, International Journal for Numerical Methods in Fluids 58 (8) (2008) 827–860.

[6] S. Xu, S. Timme, O. Mykhaskiv, J.-D. Müller, Wing-body junction optimisation with CAD-based parametrisation including a moving intersection, Aerospace Science and Technology 68 (2017) 543–551.

[7] P. Della Vecchia, E. Daniele, E. D'Amato, An airfoil shape optimization technique coupling PARSEC parameterization and evolutionary algorithm, Aerospace Science and Technology 32 (1) (2014) 103–110.

[8] D. Poole, C. Allen, T. Rendall, High-fidelity aerodynamic shape optimization using efficient orthogonal modal design variables with a constrained global optimizer, Computers & Fluids 143 (2017) 1–15.

[9] D. A. Masters, D. J. Poole, N. J. Taylor, T. Rendall, C. B. Allen, Impact of shape parameterisation on aerodynamic optimisation of benchmark problem, in: 54th AIAA Aerospace Sciences Meeting, 2016, p. 1544.

[10] M. Méheut, D. Destarac, S. Ben Khelil, G. Carrier, A. Dumont, J. Peter, Gradient-based single and multi-points aerodynamic optimizations with the elsA software, in: 53rd AIAA Aerospace Sciences Meeting, 2015, p. 0263.

[11] S. T. LeDoux, J. C. Vassberg, D. P. Young, S. Fugal, D. Kamenetskiy, W. P. Huffman, R. G. Melvin, M. F. Smith, Study based on the AIAA aerodynamic design optimization discussion group test cases, AIAA Journal 53 (7) (2015) 1910–1935.

[12] T. D. Economon, F. Palacios, S. R. Copeland, T. W. Lukaczyk, J. J. Alonso, SU2: An open-source suite for multiphysics simulation and design, AIAA Journal 54 (3) (2016) 828–846.

[13] F. Palacios, J. Alonso, K. Duraisamy, M. Colonno, J. Hicken, A. Aranake, A. Campos, S. Copeland, T. Economon, A. Lonkar, et al., Stanford University Unstructured (SU2): an open-source integrated computational environment for multi-physics simulation and design, in: 51st AIAA Aerospace Sciences Meeting, 2013, p. 287.

[14] H. Kuhn, A. Tucker, Nonlinear programming, in: Proceedings of 2nd Berkeley Symposium. Berkeley: University of California Press, 1951, pp. 481–492.

[15] W. Karush, Minima of functions of several variables with inequalities as side conditions, in: Traces and Emergence of Nonlinear Programming, Springer, 2014, pp. 217–245.

[16] A. Jameson, W. Schmidt, E. Turkel, Numerical solution of the Euler equations by finite volume methods using Runge Kutta time stepping schemes, in: 14th fluid and plasma dynamics conference, 1981, p. 1259.

[17] P. Spalart, S. Allmaras, A one-equation turbulence model for aerodynamic flows, in: 30th aerospace sciences meeting and exhibit, 1992, p. 439.

[18] R. M. Hicks, P. A. Henne, Wing design by numerical optimization, Journal of Aircraft 15 (7) (1978) 407–412.

[19] T. W. Sederberg, S. R. Parry, Free-form deformation of solid geometric models, ACM SIGGRAPH computer graphics 20 (4) (1986) 151–160.

[20] R. P. Dwight, Robust mesh deformation using the linear elasticity equations, in: Computational Fluid Dynamics 2006, Springer, 2009, pp. 401–406.

[21] A. Da Ronch, M. Panzeri, J. Drofelnik, R. d'Ippolito, Data-driven optimisation of closure coefficients of a turbulence model, in: 6th CEAS Air & Space Conference, 2017, p. 912.

[22] P. Meredith, Viscous phenomena affecting high-lift systems and suggestions for future CFD development, AGARD cp–515 (1993).

[23] G. Barakos, D. Drikakis, Numerical simulation of transonic buffet flows using various turbulence closures, International Journal of Heat and Fluid Flow 21 (5) (2000) 620–626.

[24] N. F. Giannelis, O. Levinski, G. A. Vio, Influence of Mach number and angle of attack on the two-dimensional transonic buffet phenomenon, Aerospace Science and Technology 78 (2018) 89–101.